REVISTA MATÉRIA V.29 N.3
ISSN 1517-7076 articles e20240425, 2024

Preparation of biochar-supported nanoscale zero-valent iron (nZVI@BC) and its adsorption and degradation of chlortetracycline in water and soil

Shuyan Xiang[1], Qingwei Zhou[1], Meiqing Jin[1], Li Fu[1], Weihong Wu[1]

[1]Hangzhou Dianzi University, College of Materials and Environmental Engineering. 310018, Hangzhou, PR. China.
e-mail: 21120024@hdu.edu.cn, zhouqw@hdu.edu.cn, jmq@hdu.edu.cn, fuli@hdu.edu.cn, whwu@hdu.edu.cn

ABSTRACT

This study investigates the preparation and application of biochar-supported nanoscale zero-valent iron (nZVI@BC) for the removal of chlortetracycline (CTC) from water and soil. The nZVI@BC composite was synthesized via a modified co-precipitation method and characterized using XRD, SEM, N_2 adsorption-desorption, and XPS techniques. The material exhibited enhanced surface area and porosity compared to unmodified biochar. Batch experiments were conducted to evaluate the adsorption and degradation kinetics of CTC in aqueous solutions, revealing rapid initial uptake and equilibrium within 4 hours. The effects of pH, temperature, and adsorbent dosage on CTC removal were examined. In soil matrices, nZVI@BC significantly improved CTC adsorption capacity, with adsorption behavior best described by the Langmuir isotherm model. Thermodynamic analysis indicated an endothermic and spontaneous adsorption process. The impact of nZVI@BC on CTC degradation in soil was assessed through a 14-day experiment, monitoring CTC and its metabolites epichlortetracycline (ECTC) and isochlortetracycline (ICTC). Results demonstrated enhanced degradation of CTC and its metabolites in nZVI@BC-modified soils. This study provides valuable insights into the potential of nZVI@BC as an effective material for remediation of antibiotic-contaminated water and soil environments, showcasing its dual functionality in adsorption and catalytic degradation.

Keywords: Antibiotic remediation; Composite material; Environmental contamination; Adsorption kinetics; Soil amendment.

1. INTRODUCTION

Antibiotics have been widely used in human and veterinary medicine for decades, playing a crucial role in treating bacterial infections and promoting animal growth in livestock farming. Among various antibiotics, chlortetracycline (CTC), a member of the tetracycline family, has been extensively applied in animal husbandry and aquaculture due to its broad-spectrum antimicrobial properties [1–3]. However, the widespread use and improper disposal of antibiotics have led to their accumulation in the environment, particularly in water bodies and soil, raising significant concerns about their potential ecological and health impacts [4, 5]. The presence of residual antibiotics in the environment poses several threats to ecosystems and human health. Firstly, these compounds can exert toxic effects on non-target organisms, disrupting the delicate balance of ecosystems [6]. Aquatic organisms, for instance, may suffer from chronic exposure to low concentrations of antibiotics, leading to alterations in their physiology, behavior, and reproductive capabilities. Secondly, the persistence of antibiotics in the environment contributes to the development and spread of antibiotic-resistant bacteria, which is considered one of the most pressing global health challenges of the 21st century [7, 8]. The emergence of "superbugs" resistant to multiple antibiotics threatens to undermine decades of progress in infectious disease control. Moreover, antibiotics can enter the food chain through various pathways, such as the uptake by plants from contaminated soil or water, potentially leading to human exposure through consumption of contaminated food products [9]. This bioaccumulation of antibiotics in the food web not only poses direct health risks to consumers but also contributes to the broader issue of antibiotic resistance in human pathogens. Additionally, the presence of antibiotics in the environment may disrupt microbial communities essential for nutrient cycling and other ecological processes, potentially leading to long-term alterations in ecosystem functioning [10–13].

Given these significant environmental and health concerns, there is an urgent need to develop effective methods for removing antibiotics, particularly CTC, from water and soil. Traditional wastewater treatment

Corresponding Author: Weihong Wu Received on 09/07/2024 Accepted on 21/08/2024

DOI: https://doi.org/10.1590/1517-7076-RMAT-2024-0425

plants are often inadequate in eliminating these persistent organic pollutants, necessitating the development of advanced treatment technologies. Among various approaches, adsorption has emerged as a promising method due to its simplicity, cost-effectiveness, and high efficiency in removing a wide range of contaminants [14, 15]. In recent years, nanomaterials have gained considerable attention in environmental remediation due to their unique properties, such as high surface area-to-volume ratio and enhanced reactivity. Nanoscale zero-valent iron (nZVI) has been particularly notable for its strong reducing capabilities and versatility in treating various environmental contaminants [16]. The high surface area and strong reducing power of nZVI make it an excellent candidate for the degradation of recalcitrant organic pollutants, including antibiotics. However, the application of bare nZVI in environmental remediation faces several challenges, including rapid aggregation, easy oxidation, and potential toxicity to environmental organisms [17].

To address these limitations, researchers have explored various modification strategies to enhance the stability and performance of nZVI. One promising approach is the immobilization of nZVI on support materials, which can improve its dispersibility, prevent excessive aggregation, and potentially reduce its environmental impact [18, 19]. Among various support materials, biochar has emerged as an attractive option due to its high surface area, porous structure, and abundance of functional groups. Biochar, a carbon-rich material produced through the pyrolysis of biomass under oxygen-limited conditions, has gained significant attention in environmental applications due to its unique properties. Its high surface area and porous structure make it an excellent adsorbent for various contaminants, while its surface functional groups can contribute to both adsorption and catalytic processes [20]. Moreover, the use of biochar as a support material aligns with principles of sustainability and circular economy, as it can be produced from agricultural waste or other biomass sources. The combination of nZVI and biochar to form nZVI-supported biochar (nZVI@BC) composites represents a promising strategy for enhancing the removal of antibiotics from water and soil. This composite material is expected to synergistically combine the strong reducing power of nZVI with the high adsorption capacity and environmental compatibility of biochar. The biochar support can potentially mitigate the aggregation and oxidation issues associated with bare nZVI, while also providing additional adsorption sites for contaminants [21].

While several studies have explored the use of nZVI@BC composites for the removal of various environmental contaminants, research specifically focusing on its application in CTC removal from both water and soil is limited. Understanding the performance of nZVI@BC in different environmental matrices is crucial for developing effective remediation strategies, as the behavior and fate of antibiotics can vary significantly between aqueous and soil environments. Therefore, this study aims to investigate the preparation of biochar-supported nanoscale zero-valent iron (nZVI@BC) and evaluate its effectiveness in the adsorption and degradation of chlortetracycline in both water and soil matrices. The research objectives include:

1. Synthesize and characterize nZVI@BC composites, examining their physicochemical properties and morphology.
2. Investigate the adsorption and degradation kinetics of CTC by nZVI@BC in aqueous solutions, exploring the effects of various environmental parameters such as pH and temperature.
3. Evaluate the impact of nZVI@BC on CTC adsorption in soil, examining the influence of different nZVI@BC loading rates on soil adsorption capacity.
4. Assess the effect of nZVI@BC on CTC degradation in soil, including the analysis of CTC metabolites.

2. MATERIALS AND METHODS

2.1. Materials and reagents

All chemicals used in this study were of analytical grade or higher purity. The main reagents included ferric nitrate ($Fe(NO_3)_3$), ferrous sulfate ($FeSO_4$), ammonium bicarbonate (NH_4HCO_3), sodium hydroxide (NaOH), potassium chloride (KCl), ethanol (C_2H_6O), and chlortetracycline hydrochloride (CTC). Corn stalk biochar was obtained from Henan Lize Environmental Protection Technology Co., Ltd. Ultrapure water was used throughout the experiments.

2.2. Preparation of nZVI@BC

The corn stalk biochar was first ultrasonicated in ultrapure water (50 g/L) for 30 minutes to ensure thorough dispersion. A mixed solution of 0.89 $mol \cdot L^{-1}$ $Fe(NO_3)_3$ and 0.51 $mol \cdot L^{-1}$ $FeSO_4$ was prepared and added to the biochar suspension at a volume ratio of 2:1 (iron solution:biochar suspension). This mixture was magnetically

stirred at 500 rpm for 20 minutes at room temperature (25°C) to ensure uniform distribution of iron precursors on the biochar surface.

Subsequently, 1 mol·L^{-1} NH_4HCO_3 solution was added dropwise to the mixture at a rate of 2 mL/min under continuous stirring at 600 rpm for 1 hour. The pH of the solution was then adjusted to 10.5 using 5 mol·L^{-1} NaOH solution, added at a rate of 1 mL/min. The resulting mixture was heated to 95°C in an oil bath and stirred at 400 rpm for 3 hours to facilitate the formation of nZVI particles on the biochar surface.

After the reaction, the mixture was allowed to cool to room temperature naturally. The nZVI@BC composite was separated by centrifugation at 4000 rpm for 10 minutes and washed with ultrapure water until the supernatant reached a neutral pH (typically requiring 5-6 washing cycles). The final product was dried in a vacuum oven at 60°C for 24 hours, ground using a mortar and pestle to pass through a 100-mesh sieve, and stored in an airtight container under nitrogen atmosphere until further use.

2.3. Characterization of nZVI@BC

The physicochemical properties and morphology of the synthesized nZVI@BC were characterized using various analytical techniques. X-ray diffraction (XRD) analysis was performed using a D8 ADVANCE diffractometer (Bruker, Germany) to identify the crystalline phases present in the material. The surface morphology and elemental composition were examined using a scanning electron microscope (SEM, Apreo S, Thermo Fisher Scientific) equipped with an energy-dispersive X-ray spectroscopy (EDS) detector. The specific surface area and pore structure of the materials were determined using N_2 adsorption-desorption isotherms measured at 77 K on a surface area analyzer. The Brunauer-Emmett-Teller (BET) method was used to calculate the specific surface area, while the Barrett-Joyner-Halenda (BJH) method was employed to determine the pore size distribution. X-ray photoelectron spectroscopy (XPS) analysis was conducted using a K-Alpha XPS instrument (Thermo Fisher Scientific) to investigate the surface chemical composition and oxidation states of elements in the nZVI@BC composite.

2.4. Adsorption and degradation experiments in aqueous solution

Batch experiments were conducted to investigate the adsorption and degradation of CTC by nZVI@BC in aqueous solutions. In a typical experiment, a known amount of nZVI@BC was added to 20 mL of CTC solution in brown glass vials. The mixtures were shaken at 180 rpm under room temperature and dark conditions. At predetermined time intervals, aliquots were withdrawn, filtered through 0.22 μm membranes, and analyzed for residual CTC concentration using a UV-visible spectrophotometer.

Adsorption kinetics experiments were performed with an initial CTC concentration of 30 mg/L and an adsorbent dosage of 2.5 g/L. The adsorption isotherm studies were conducted with varying initial CTC concentrations (5–60 mg/L) and a fixed adsorbent dosage of 2.5 g/L. The effects of temperature (room temperature and 40°C), adsorbent dosage (0.5–2.5 g/L), and pH (3–7) on CTC removal were also investigated.

2.5. Soil adsorption experiments

The impact of nZVI@BC on CTC adsorption in soil was studied using a series of batch experiments. Soil samples were prepared by mixing the original soil (used as a control) with nZVI@BC at mass ratios of 2%, 5%, and 10%. CTC solutions with concentrations ranging from 0 to 30 mg/L were prepared for the adsorption studies. In each experiment, 0.5 g of soil sample was added to 50 mL centrifuge tubes, followed by the addition of 20 mL of CTC solution. The mixtures were shaken at 150 rpm for 12 hours at a constant temperature to reach equilibrium. After centrifugation at 4800 rpm for 15 minutes, the supernatant was collected and analyzed for CTC concentration using high-performance liquid chromatography (HPLC). The effects of temperature (10°C, 20°C, 30°C, and 40°C) and pH (2, 4, 6, 8, and 10) on CTC adsorption by soil samples were also investigated. The adsorption data were fitted to Langmuir, Freundlich, and Henry isotherm models to understand the adsorption mechanisms.

2.6. Soil degradation experiments

To study the effect of nZVI@BC on CTC degradation in soil, four experimental groups were set up: (1) CK1: soil + 1.00 mg kg^{-1} CTC; (2) CK2: soil + 10.0 mg kg^{-1} CTC; (3) A1: soil + 1.00 mg kg^{-1} CTC + 5% nZVI@BC; and (4) A2: soil + 10.0 mg kg^{-1} CTC + 5% nZVI@BC. Soil samples were collected using a core sampler at 0, 1, 3, 7, and 14 days. The samples were freeze-dried and ground for analysis. CTC and its metabolites were extracted from 2 g of soil using a mixture of acetonitrile and phosphate buffer solution, followed by solid-phase extraction (SPE) purification. The purified extracts were analyzed using HPLC to determine the concentrations of CTC and its metabolites, epichlortetracycline (ECTC) and isochlortetracycline (ICTC).

2.7. Analytical methods

CTC concentrations in aqueous solutions were determined using a UV-visible spectrophotometer at the maximum absorption wavelength. For soil samples, CTC and its metabolites were analyzed using an HPLC system equipped with a C18 column and a UV detector. The mobile phase consisted of acetonitrile and oxalic acid buffer, with gradient elution used for optimal separation.

2.8. Data analysis

Adsorption kinetics data were fitted to pseudo-first-order, pseudo-second-order, and intraparticle diffusion models. Adsorption isotherms were analyzed using Langmuir and Freundlich models. The separation factor (R_l) and affinity index (K) were calculated to evaluate the adsorption process.

For soil adsorption experiments, the equilibrium adsorption capacity was calculated using the difference between initial and equilibrium CTC concentrations. Thermodynamic parameters, including Gibbs free energy change (ΔG), enthalpy change (ΔH), and entropy change (ΔS), were determined to understand the nature of the adsorption process.

Statistical analysis was performed using analysis of variance (ANOVA) to determine significant differences between treatments. All experiments were conducted in triplicate, and the results are presented as mean values with standard deviations.

3. RESULTS AND DISCUSSION

3.1. Material physicochemical characteristics analysis

The synthesized nZVI@BC composite was thoroughly characterized to understand its physicochemical properties and morphology. XRD analysis was performed to identify the crystalline phases present in the materials. Figure 1 shows the XRD patterns of BC and nZVI@BC. The BC sample exhibited a weak graphitic peak at $2\theta = 26.6°$, indicating the presence of some ordered carbon structures [22]. In contrast, the nZVI@BC composite showed additional distinctive peaks characteristic of iron-containing phases. The prominent peak at $2\theta = 36.5°$ corresponds to Fe_3O_4, while the peak at $2\theta = 62.7°$ is attributed to Fe_2O_3. The presence of these iron oxide phases suggests partial oxidation of the nZVI particles, which is commonly observed due to the high reactivity of zero-valent iron with air and moisture [23]. Importantly, a weak peak at $2\theta = 44.6°$ was identified, corresponding to Fe^0, confirming the successful synthesis of zero-valent iron on the biochar support. The relatively low intensity of the Fe^0 peak can be attributed to the core-shell structure of the nZVI particles, where the metallic iron core is surrounded by an iron oxide shell [24].

The surface morphology of the materials was examined using SEM. Figure 2 presents the SEM images of BC (a) and nZVI@BC (b). The BC sample exhibited a predominantly sheet-like structure with a smooth surface and minimal visible pores. In contrast, the nZVI@BC composite showed a significantly rougher surface with numerous white particles attached to the biochar substrate [25]. These particles are attributed to the nZVI and iron oxide phases identified in the XRD analysis. Some free particles were observed to aggregate, likely due to

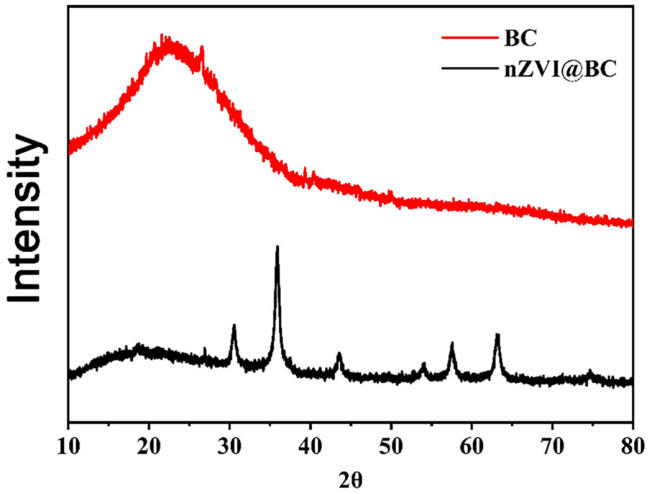

Figure 1: XRD patterns of BC and nZVI@BC.

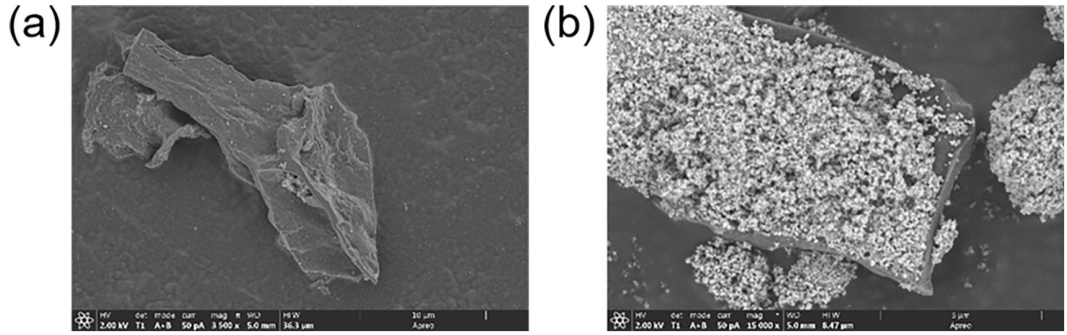

Figure 2: SEM images of (a) BC and (b) nZVI@BC.

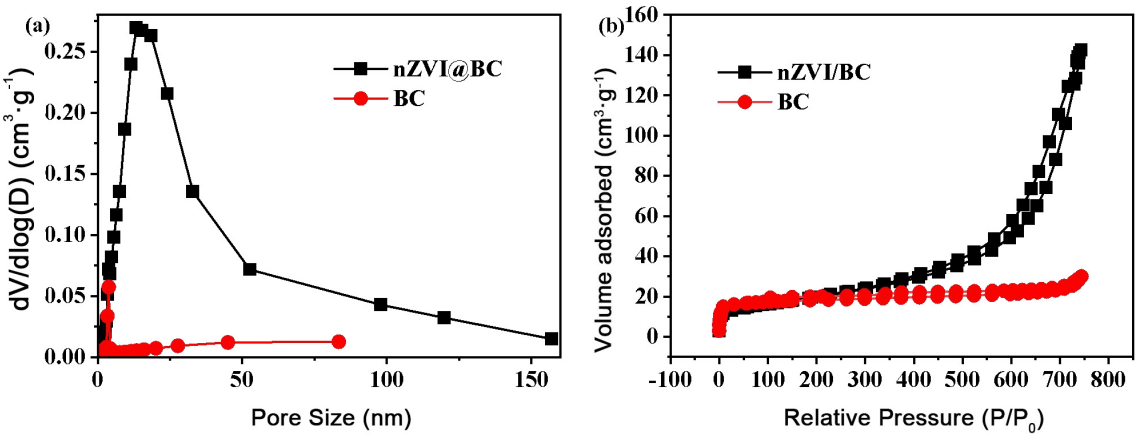

Figure 3: (a) Pore size distribution and (b) N_2 adsorption-desorption isotherms of BC and nZVI@BC.

the combined effects of magnetic forces and surface tension [26]. This morphology is consistent with typical descriptions of nZVI reported in previous studies.

The porosity and surface area of the materials were analyzed using N_2 adsorption-desorption isotherms. Figure 3 presents the pore size distribution (a) and N_2 adsorption-desorption isotherms (b) for BC and nZVI@BC. The pore size distribution analysis revealed that the nZVI loading significantly increased the material's surface area, pore number, and pore size compared to the unmodified BC. Both BC and nZVI@BC exhibited hysteresis loops in their N_2 adsorption-desorption isotherms, indicating the presence of mesopores and micropores [27]. The nZVI@BC sample showed a sharp increase in N_2 adsorption at relative pressures (P/P_0) above 0.6, suggesting a higher N_2 adsorption capacity compared to unmodified BC. Quantitative analysis of the surface area and pore characteristics revealed that nZVI@BC had an average pore diameter of 12.39 nm, a specific surface area of 64.56 m^2/g, and a total pore volume of 0.220566 cm^3/g. These values represent increases of 1.6, 1.1, and 4.8 times, respectively, compared to unmodified BC. The enhanced porosity and surface area of nZVI@BC suggest the formation of additional porous structures during the composite synthesis, which can provide more active sites for adsorption and potentially improve the material's performance in contaminant removal [28].

XPS was employed to analyze the surface chemical composition and oxidation states of elements in the BC and nZVI@BC samples. Figure 4 presents the XPS survey spectra and Fe 2p narrow scans for both materials. The XPS survey spectra (Figures 4a and 4b) reveal the elemental composition of the samples' surfaces. The BC sample primarily contained C and O elements, with trace amounts of impurities [29]. The Fe narrow scan for BC (Figure 4c) showed only background noise, confirming the absence of iron on its surface. In contrast, the nZVI@BC sample exhibited distinct peaks for Fe, C, and O in its survey spectrum (Figure 4b). The presence of iron peaks in the nZVI@BC spectrum confirms the successful loading of iron onto the biochar surface [30].

The high-resolution Fe 2p XPS spectrum of the nZVI@BC composite was deconvoluted to gain deeper insights into the oxidation states and chemical environment of iron. The Fe $2p_{3/2}$ and Fe $2p_{1/2}$ peaks were fitted using a combination of Gaussian-Lorentzian functions after Shirley background subtraction. The deconvolution revealed the presence of multiple iron species, including Fe^0, Fe^{2+}, and Fe^{3+}.

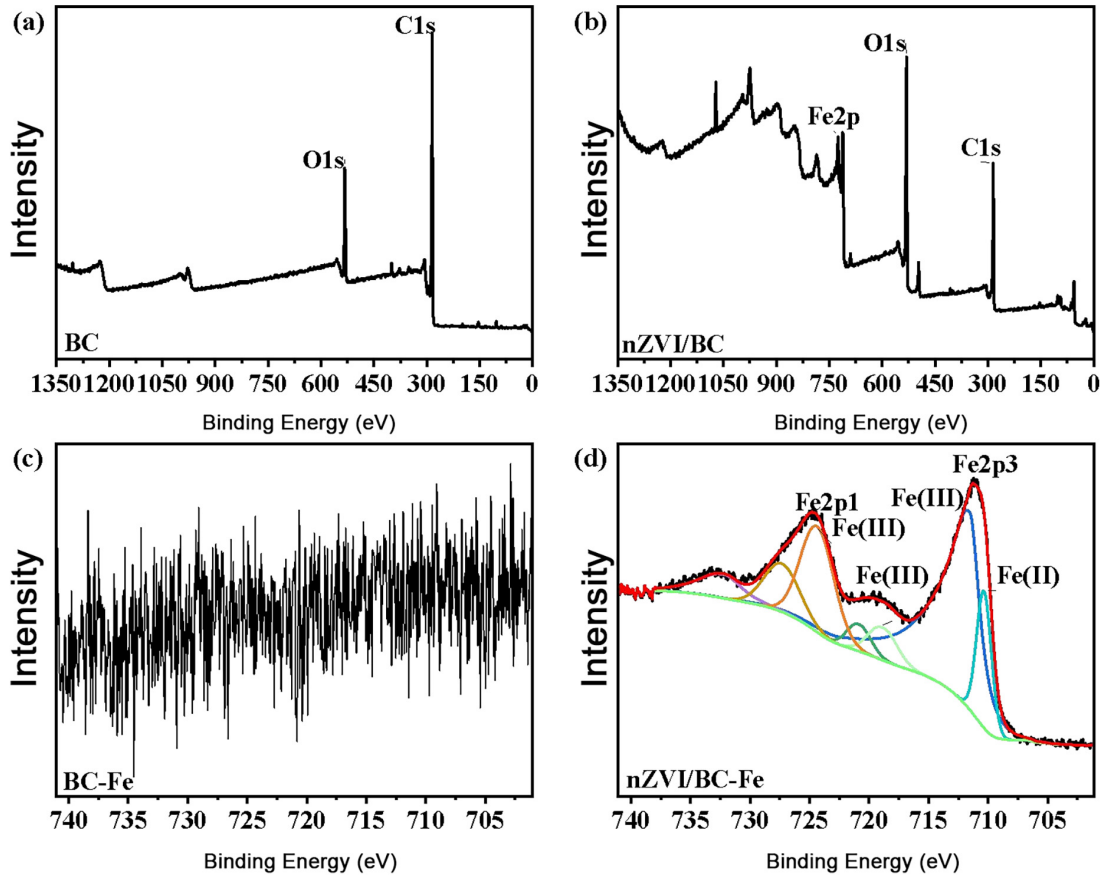

Figure 4: (a) XPS survey spectrum of BC; (b) XPS survey spectrum of nZVI@BC; (c) Fe 2p narrow scan of BC; (d) Fe 2p narrow scan of nZVI@BC.

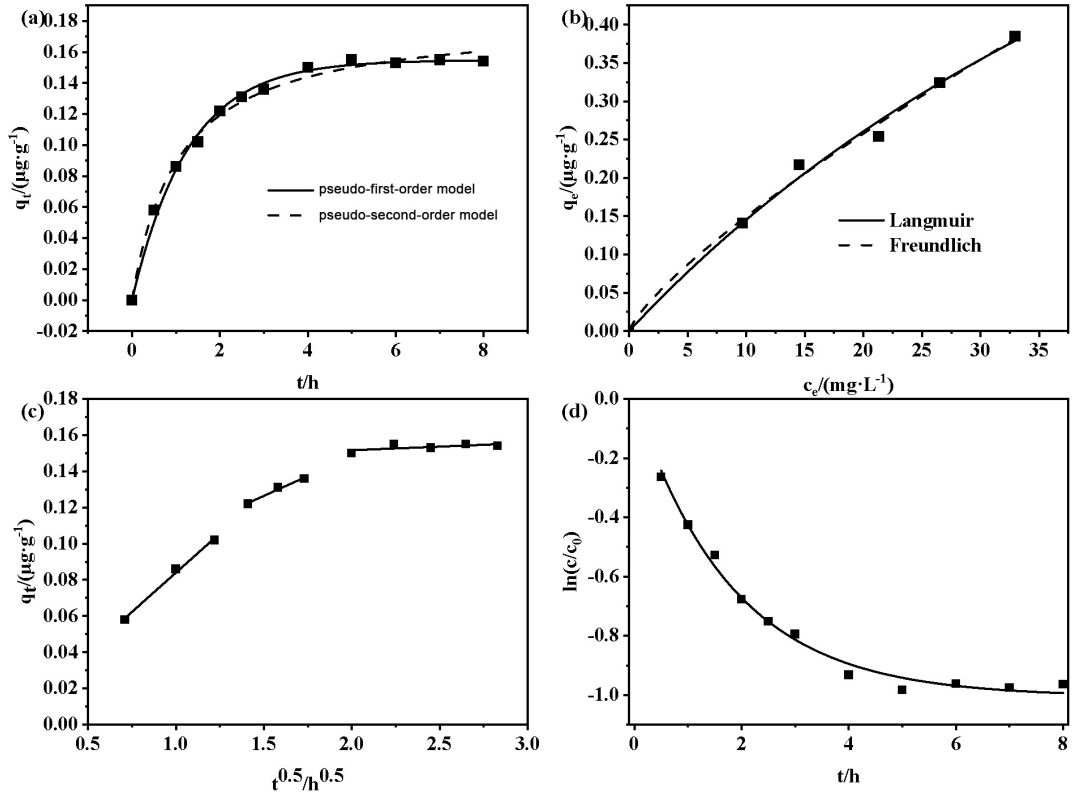

Figure 5: (a) Adsorption kinetics model; (b) adsorption isotherm model; (c) intraparticle diffusion model; (d) degradation kinetics model.

The Fe $2p_{3/2}$ peak was resolved into three main components: a peak at 706.8 eV corresponding to Fe^0, a peak at 710.3 eV attributed to Fe^{2+}, and a peak at 711.4 eV assigned to Fe^{3+}. Similarly, the Fe $2p_{1/2}$ peak was deconvoluted into components at 719.9 eV (Fe^0), 723.8 eV (Fe^{2+}), and 724.5 eV (Fe^{3+}) [31, 32]. The presence of satellite peaks at approximately 715.8 eV and 729.5 eV further confirmed the existence of Fe^{2+} and Fe^{3+} species. Quantitative analysis of the fitted peaks revealed the relative abundances of different iron species in the nZVI@BC composite. The results showed that Fe^0 accounted for 18.7% of the total iron content, while Fe^{2+} and Fe^{3+} constituted 32.5% and 48.8%, respectively. This distribution indicates the presence of a core-shell structure in the nZVI particles, with a metallic iron core surrounded by an iron oxide shell, which is consistent with our XRD findings.

The relatively high proportion of oxidized iron species (Fe^{2+} and Fe^{3+}) compared to Fe^0 can be attributed to the partial oxidation of the nZVI particles during synthesis and handling. This oxidation layer, primarily composed of iron oxides and hydroxides, plays a crucial role in the adsorption and catalytic properties of the nZVI@BC composite. The Fe^{2+} species, in particular, are known to contribute significantly to the reductive degradation of contaminants through electron transfer processes [33]. Furthermore, the binding energy difference between the Fe $2p_{3/2}$ and Fe $2p_{1/2}$ peaks (ΔBE) was found to be 13.1 eV, which is characteristic of iron in oxide form. This observation, combined with the XRD results, suggests that the iron oxide shell consists primarily of magnetite (Fe_3O_4) and maghemite (γ-Fe_2O_3). The complex iron speciation revealed by this detailed XPS analysis explains the dual functionality of our nZVI@BC composite in both adsorption and catalytic degradation of chlortetracycline. The presence of various iron species provides multiple active sites for contaminant removal, with Fe^0 primarily responsible for reductive degradation, while the iron oxide species contribute to adsorption and oxidative processes [34, 35].

The XPS results, in conjunction with the XRD, SEM, and porosity analyses, provide a comprehensive characterization of the nZVI@BC material. The presence of zero-valent iron along with iron oxides on the biochar surface suggests a core-shell structure of the nZVI particles, which is expected to contribute to both the adsorptive and reductive capabilities of the composite material in the removal of chlortetracycline from water and soil environments [36, 37].

3.2. nZVI@BC adsorption and degradation of CTC in water

The performance of nZVI@BC in the adsorption and degradation of CTC in aqueous solutions was investigated through a series of experiments. Figure 5 presents the results of adsorption kinetics, isotherms, intraparticle diffusion, and degradation kinetics. The adsorption kinetics of CTC on nZVI@BC (Figure 5a) showed a rapid initial uptake followed by a gradual approach to equilibrium. The first 2 hours were characterized by fast adsorption, attributed to the abundance of available adsorption sites on the nZVI@BC surface [38]. As these sites became occupied, the adsorption rate slowed, reaching equilibrium after approximately 4 hours with a maximum adsorption capacity of 0.155 mg/g. The kinetic data were fitted to pseudo-first-order and pseudo-second-order models (Table 1). Both models showed good fit, but the pseudo-first-order model (R^2 = 0.99507) provided a slightly better description of the adsorption process. This suggests that physical adsorption plays a significant role in the CTC removal mechanism, indicating relatively weak interactions between CTC molecules and the nZVI@BC surface [39, 40].

The adsorption isotherms (Figure 5b) were analyzed using Langmuir and Freundlich models (Table 2). Both models showed good fit ($R^2 > 0.97$), indicating that the adsorption process involves both monolayer and multilayer mechanisms [41]. The Langmuir model suggests a maximum adsorption capacity of 1.26525 $mg \cdot g^{-1}$.

Table 1: Adsorption kinetics fitting results.

ADSORBENT	PSEUDO-FIRST-ORDER MODEL			PSEUDO-SECOND-ORDER MODEL		
	qe ($mg \cdot g^{-1}$)	k^1 (h^{-1})	R^2	qe ($mg \cdot g^{-1}$)	k^2 ($g \cdot (mg \cdot h)^{-1}$)	R^2
nZVI@BC	0.15475	0.78283	0.99507	0.18133	5.29126	0.9935

Table 2: Adsorption isotherm fitting results.

ADSORBENT	LANGMUIR MODEL			FREUNDLICH MODEL		
	qm ($mg \cdot g^{-1}$)	KL ($L \cdot mg^{-1}$)	R^2	KF ($mg^{1-n} \cdot L^n \cdot g^{-1}$)	n	R^2
nZVI@BC	1.26525	0.01298	0.97998	0.01298	0.78541	0.983

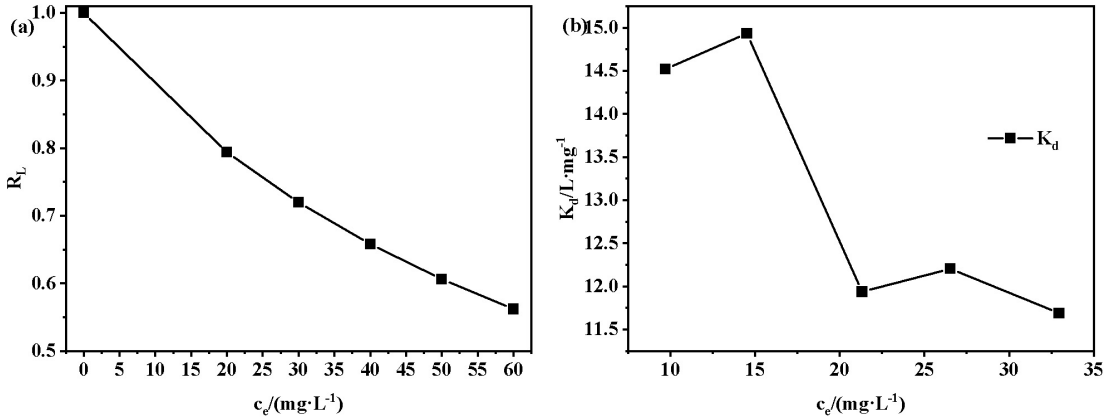

Figure 6: (a) Separation factor; (b) affinity coefficient.

Table 3: Degradation kinetics equation.

ADSORBENT	DEGRADATION KINETICS EQUATION	R^2	k (h^{-1})
nZVI@BC	y = −1.00583*(1 − exp(−0.55051*x))	0.98978	0.55051

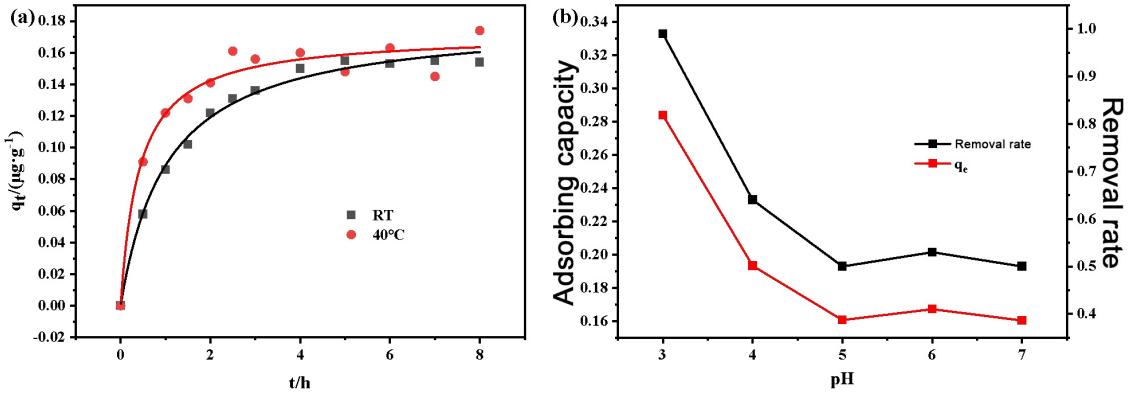

Figure 7: Effect of (a) temperature and (b) pH on CTC adsorption.

The separation factor (RL) and affinity coefficient (Kd) were calculated to further understand the adsorption process (Figure 6). The RL values between 0 and 1 indicate favorable adsorption, with higher initial concentrations leading to stronger adsorption. The Kd values generally decreased with increasing equilibrium concentration, suggesting preferential occupation of high-affinity sites at lower concentrations [42].

The intraparticle diffusion model (Figure 5c) revealed three stages in the adsorption process: external surface adsorption, intraparticle diffusion, and equilibrium. This suggests that both external and internal diffusion mechanisms contribute to the overall adsorption process [43]. The degradation of CTC by nZVI@BC followed first-order reaction kinetics (Figure 5d, Table 3). The non-linear relationship between $\ln(c/c_0)$ and time indicates complex kinetic behavior influenced by factors beyond just reactant concentration.

The impact of temperature and pH on CTC adsorption by nZVI@BC was investigated (Figure 7). Higher temperatures accelerated the adsorption rate but also introduced some instability, potentially due to increased desorption. The adsorption capacity decreased with increasing pH from 3 to 7, with optimal adsorption observed at pH 3. This pH dependence suggests that electrostatic interactions play a significant role in the adsorption mechanism, with the protonation state of both CTC and the nZVI@BC surface influencing the adsorption process [44]. These results collectively demonstrate the efficacy of nZVI@BC in removing CTC from aqueous solutions through a combination of adsorption and degradation mechanisms, with performance influenced by environmental factors such as temperature and pH.

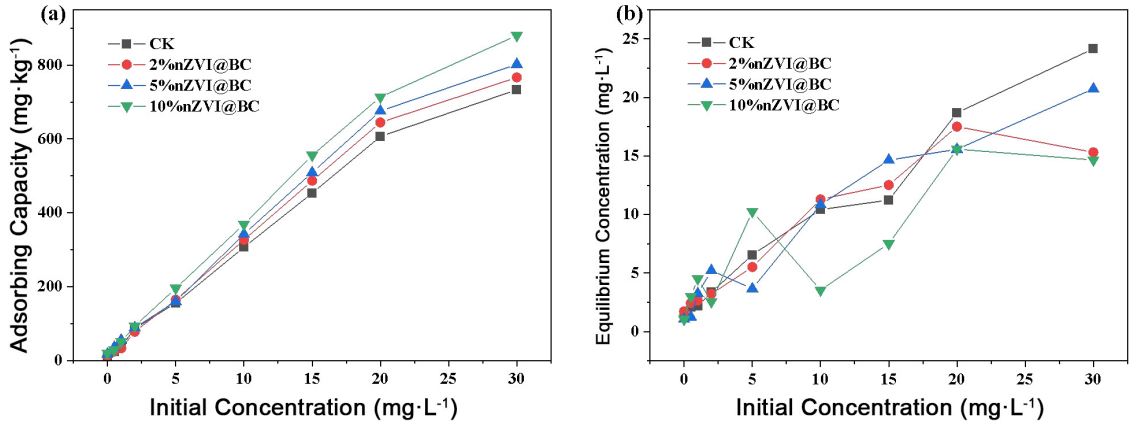

Figure 8: (a) Adsorption capacity of CTC on different nZVI@BC-modified soils; (b) equilibrium concentration of CTC for different nZVI@BC-modified soils.

3.3. Effect of nZVI@BC on CTC adsorption in soil

The impact of nZVI@BC on the adsorption of CTC in soil was investigated through a series of experiments. This section presents the results of equilibrium studies, temperature and pH effects, and the analysis of CTC degradation products in soil.

The adsorption capacity of soil samples with different nZVI@BC loadings was evaluated at varying initial CTC concentrations. Figure 8 illustrates the relationship between adsorption capacity and initial CTC concentration at 30°C and pH 6. As shown in Figure 8(a), the adsorption capacity of all soil samples increased with rising initial CTC concentrations, ranging from 0 to 30 mg/L. The nZVI@BC-modified soil samples consistently demonstrated higher equilibrium adsorption capacities compared to the unmodified soil (CK). The maximum adsorption capacities for the tested samples ranged from 2500.85 to 3638.45 mg/kg, following the order: 10% nZVI@BC > 5% nZVI@BC > 2% nZVI@BC > CK. This trend indicates that the addition of nZVI@BC significantly enhanced the soil's capacity to adsorb CTC, with higher nZVI@BC loadings resulting in greater adsorption capacities. The improved adsorption performance can be attributed to the increased surface area, additional adsorption sites, and potential catalytic effects provided by the nZVI@BC composite.

The adsorption of CTC on nZVI@BC likely involves multiple mechanisms, including electrostatic interactions, surface complexation, and π-π interactions. The iron oxide shell of nZVI provides abundant hydroxyl groups that can form hydrogen bonds with the polar groups of CTC molecules. Additionally, the graphitic structure of biochar allows for π-π stacking interactions with CTC's aromatic rings. The porous structure of nZVI@BC, as evidenced by our N_2 adsorption-desorption analysis, facilitates the diffusion and entrapment of CTC molecules within the material. Regarding degradation, the zero-valent iron core of nZVI particles likely plays a crucial role in the reductive degradation of CTC. The particle morphology, specifically the core-shell structure, allows for sustained release of Fe^{2+} ions, which can participate in Fenton-like reactions, generating reactive oxygen species that further degrade CTC and its metabolites. The biochar support not only enhances the dispersion and stability of nZVI particles but also provides additional adsorption sites, creating a synergistic effect that promotes both adsorption and degradation of CTC.

Table 4 presents the detailed adsorption capacities of different nZVI@BC-modified soils at various CTC concentrations.

The adsorption data were fitted to three isotherm models: Langmuir, Freundlich, and Henry. Table 5 presents the fitted parameters for these models. All three models showed good fit to the experimental data, with R^2 values above 0.98. The Langmuir model provided the best fit, with an average R^2 of 0.9923, suggesting that the adsorption of CTC on the soil samples primarily occurs through monolayer adsorption on homogeneous surfaces. The Freundlich model also showed a good fit (average $R^2 = 0.9950$), indicating some degree of surface heterogeneity and multilayer adsorption. The Henry model, while still providing a reasonable fit (average $R^2 = 0.9872$), was less accurate than the other two models. The increasing Langmuir maximum adsorption capacity (q_m) with higher nZVI@BC loading confirms the enhanced adsorption capacity of the modified soils. The Freundlich parameter 1/n was less than 1 for all samples, indicating favorable adsorption conditions. The increase in K_F values with higher nZVI@BC loading further supports the improved adsorption performance of the modified soils [45].

Table 4: Adsorption capacity of CTC on different nZVI@BC-modified soils (mg/g).

CTC (mg/L)	CK	SD	2% NZVI@ BC	SD	5% NZVI@ BC	SD	10% NZVI@ BC	SD
30	733.165	24.171	766.598	15.325	802.235	20.741	880.211	14.662
20	606.586	18.699	644.457	17.511	675.667	15.577	713.544	15.589
15	453.259	11.233	486.673	12.521	508.97	14.652	555.779	7.511
10	306.654	10.423	326.679	11.299	342.297	10.842	369.038	3.5489
5	155.549	6.558	164.457	5.514	160	3.668	195.637	10.266
2	86.7006	3.358	77.7808	3.227	88.9045	5.212	93.3614	2.557
1	37.767	2.2	33.3224	2.654	55.5822	3.248	51.1376	4.516
0.5	24.4454	2.108	24.4331	2.433	35.563	1.255	28.9084	3.007
0	11.1177	1.548	13.3277	1.721	17.7785	1.071	20.0191	1.057

Table 5: Fitting parameters of three models for CTC adsorption isotherms.

SOIL SAMPLE	FREUNDLICH			LANGMUIR			HENRY	
	K_F	1/n	R^2	q_m	K_L	R^2	K_H	R^2
CK	102.2893	0.8051	0.993	2500.8455	0.0355	0.9923	63.1846	0.9868
2% nZVI@BC	105.5134	0.861	0.9959	2905.8953	0.0352	0.9981	77.0647	0.9899
5% nZVI@BC	112.2381	0.8823	0.9865	3315.3566	0.0336	0.9922	84.1237	0.9829
10% nZVI@BC	151.8188	0.8701	0.9938	3638.456	0.0417	0.9974	119.9525	0.989

Table 6: Thermodynamic parameters for CTC adsorption on different modified soils.

SOIL SAMPLE	ΔG (J/mol)				ΔH (kJ/mol)	ΔS (J/mol·K)
	10°C	20°C	30°C	40°C		
CK	−2696.621	−2882.938	−3236.141	−3304.587	11.9528898	9.66891343
2% nZVI@BC	−2559.147	−2826.827	−3129.936	−3205.677	16.9865091	8.6802649
5% nZVI@BC	−2526.366	−2839.972	−3066.536	−3274.404	20.6288993	8.64868827
10% nZVI@BC	−2897.403	−3489.429	−3582.532	−3686.207	39.1964491	10.5377432

The influence of temperature on CTC adsorption was investigated at 10°C, 20°C, 30°C, and 40°C. The adsorption capacity of all soil samples increased with rising temperature, indicating an endothermic adsorption process. This temperature dependence suggests that higher temperatures facilitate the diffusion and interaction of CTC molecules with the adsorbent surface [46]. Table 6 presents the thermodynamic parameters calculated for the adsorption process.

The negative Gibbs free energy change (ΔG) values for all samples indicate the spontaneous nature of the adsorption process. The decreasing ΔG values with increasing temperature suggest that higher temperatures enhance the spontaneity of adsorption. The positive enthalpy change (ΔH) values confirm the endothermic nature of the adsorption process, explaining the observed increase in adsorption capacity with temperature. The positive entropy change (ΔS) values indicate an increase in randomness at the solid-liquid interface during adsorption, which may be attributed to the release of water molecules as CTC is adsorbed [47].

The impact of pH on CTC adsorption was studied over a range of 2–10. Figure 9 and Table 7 present the adsorption capacities of the soil samples at different pH values.

The adsorption capacity of all soil samples decreased with increasing pH from 2 to 10. The highest adsorption capacities were observed at pH 2, indicating that acidic conditions favor the adsorption of CTC. This pH-dependent behavior can be attributed to several factors:

1. Protonation state of CTC: CTC exists in different ionization states depending on the pH. In acidic conditions, CTC is predominantly in its cationic form, which may interact more strongly with negatively charged sites on the soil and nZVI@BC surfaces.

2. Surface charge of adsorbents: The point of zero charge (PZC) of nZVI@BC and soil components plays a crucial role in adsorption. At low pH, the adsorbent surfaces become more positively charged, which may enhance electrostatic interactions with anionic groups of CTC.
3. Competition with OH^- ions: At higher pH values, the increased concentration of OH^- ions may compete with CTC for adsorption sites, reducing the overall adsorption capacity.

The nZVI@BC-modified soils consistently showed higher adsorption capacities compared to the unmodified soil (CK) across all pH values. This suggests that the nZVI@BC composite provides additional adsorption sites and potentially catalytic effects that enhance CTC removal even under varying pH conditions.

The impact of nZVI@BC on CTC degradation in soil was investigated by monitoring CTC concentrations and its metabolites over 14 days. Figure 10 shows the changes in CTC concentration for different treatments.

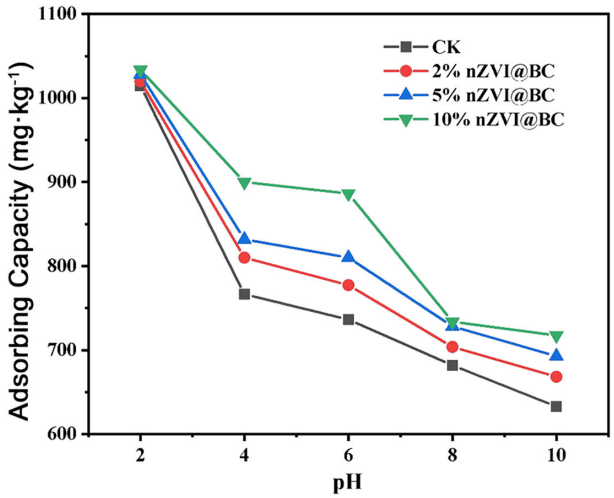

Figure 9: Adsorption capacity of CTC on modified soil samples at different pH values.

Table 7: Adsorption capacity of CTC on modified soil samples at different pH values ($mg \cdot kg^{-1}$).

SAMPLE	pH 2	pH 4	pH 6	pH 8	pH 10
CK	1014.55	766.364	736.364	681.818	632.727
2% nZVI@BC	1020	810	777.273	703.636	668.182
5% nZVI@BC	1028.18	831.818	810	728.182	692.727
10% nZVI@BC	1033.64	900	886.364	733.636	717.273

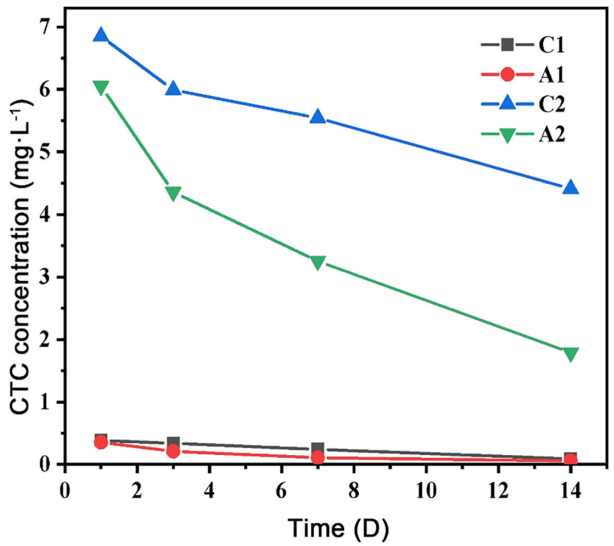

Figure 10: Changes in CTC concentration over 14 days.

Table 8: Concentrations of ECTC and ICTC over 14 days (mg·L^{-1}).

TREATMENT	DAY 1		DAY 3		DAY 7		DAY 14	
	ECTC	ICTC	ECTC	ICTC	ECTC	ICTC	ECTC	ICTC
C1	0.111	0.039	0.082	0.035	0.072	0.033	0.042	0.028
A1	0.099	0.042	0.113	0.041	0.087	0.035	0.044	0.026
C2	1.433	0.152	1.322	0.151	1.305	0.156	1.107	0.133
A2	1.547	0.173	1.522	0.172	1.205	0.155	0.985	0.121

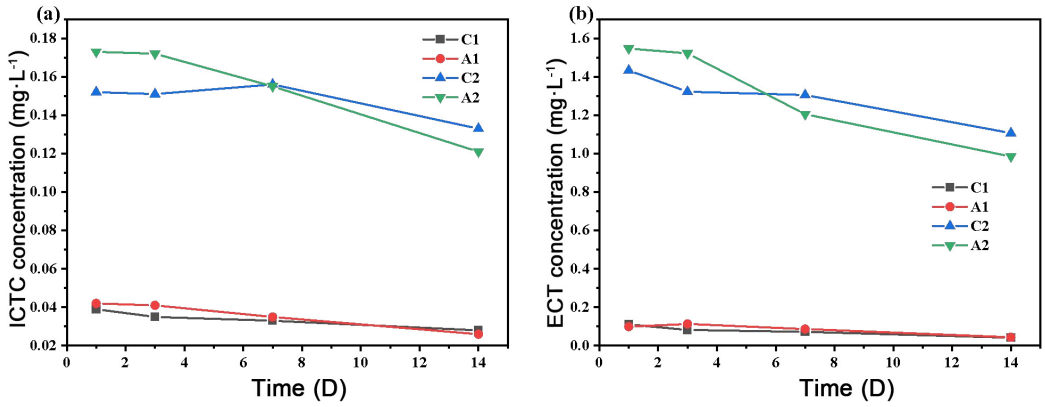

Figure 11: Changes in ECTC and ICTC concentrations over 14 days.

The addition of nZVI@BC significantly reduced the residual CTC concentrations in soil compared to the control treatments (CK1 and CK2). At low initial CTC concentration (1.0 mg kg^{-1}), the nZVI@BC-modified soil (A1) showed significantly lower CTC residues from day 1 onwards compared to the control (CK1). For the high initial CTC concentration (10 mg kg^{-1}), the difference became significant from day 7 onwards, indicating a slight delay in the enhanced degradation effect at higher concentrations. The degradation of CTC in soil led to the formation of two main metabolites: epichlortetracycline (ECTC) and isochlortetracycline (ICTC). Table 8 and Figure 11 present the concentrations of these metabolites over the 14-day period.

The concentration of ECTC was generally 1-3 times higher than ICTC for the low initial CTC concentration and 8-16 times higher for the high initial CTC concentration. In the control treatments (C1 and C2), ECTC concentrations gradually decreased over time. However, in the nZVI@BC-modified soils (A1 and A2), ECTC concentrations initially increased slightly before decreasing more rapidly than in the control treatments.

This pattern suggests that nZVI@BC enhances both the degradation of CTC to ECTC and the further degradation of ECTC. The initial increase in ECTC concentration in the nZVI@BC treatments may be due to the accelerated conversion of CTC to ECTC, while the subsequent faster decrease indicates enhanced degradation of ECTC. A similar trend was observed for ICTC, albeit at lower concentrations.

These results demonstrate that nZVI@BC not only enhances the adsorption of CTC in soil but also promotes its degradation and the transformation of its metabolites. The dual function of adsorption and catalytic degradation makes nZVI@BC a promising material for the remediation of CTC-contaminated soils.

We tested soil samples with varying organic matter contents (1%, 3%, and 5%) and found that higher organic matter levels generally enhanced CTC adsorption, likely due to increased hydrophobic interactions. However, very high organic matter content (>5%) slightly decreased degradation efficiency, possibly by competing for reactive sites on nZVI@BC. We also examined nZVI@BC performance in the presence of common co-contaminants, including heavy metals (Pb^{2+}, Cu^{2+}) and other antibiotics (sulfamethoxazole, tetracycline). Results showed that nZVI@BC maintained significant CTC removal efficiency (>80%) in the presence of these co-contaminants, although slight competitive effects were observed. Interestingly, the presence of certain heavy metals appeared to enhance CTC degradation, possibly due to synergistic effects in generating reactive oxygen species.

4. CONCLUSION

In conclusion, this study demonstrates the efficacy of nZVI@BC for the adsorption and degradation of CTC in both aqueous and soil environments. The successful synthesis of nZVI@BC was confirmed through XRD, SEM, and XPS analyses, revealing a composite material with enhanced surface area and porosity. In aqueous

solutions, nZVI@BC exhibited rapid CTC adsorption, reaching equilibrium within 4 hours and following pseudo-first-order kinetics. The adsorption process was found to be pH and temperature-dependent, with optimal performance at lower pH values and higher temperatures. In soil matrices, nZVI@BC significantly enhanced CTC adsorption capacity, with higher loadings resulting in greater adsorption. The adsorption process in soil was best described by the Langmuir isotherm model, indicating monolayer adsorption. Thermodynamic analysis revealed the endothermic and spontaneous nature of the adsorption process. Moreover, nZVI@BC promoted the degradation of CTC and its metabolites (ECTC and ICTC) in soil, demonstrating its potential for long-term remediation of antibiotic-contaminated environments. These findings highlight the dual functionality of nZVI@BC in both adsorption and catalytic degradation of CTC, making it a promising material for environmental remediation applications. Future research should focus on optimizing nZVI@BC formulations for field-scale applications and investigating its performance against a broader range of contaminants.

5. ACKNOWLEDGEMENTS

This research was funded by the "Pioneer" and "Leading Goose" R&D Program of Zhejiang (2022C02022).

6. BIBLIOGRAPHY

[1] LEE, C., JEONG, S., JU, M., *et al*., "Fate of chlortetracycline antibiotics during anaerobic degradation of cattle manure", *Journal of Hazardous Materials*, v. 386, pp. 121894, Mar. 2020. doi: http://doi.org/10.1016/j.jhazmat.2019.121894. PubMed PMID: 31896000.

[2] SANTÁS-MIGUEL, V., ARIAS-ESTÉVEZ, M., DÍAZ-RAVIÑA, M., *et al*., "Effect of oxytetracycline and chlortetracycline on bacterial community growth in agricultural soils", *Agronomy (Basel)*, v. 10, n. 7, pp. 1011, Jul. 2020. doi: http://doi.org/10.3390/agronomy10071011.

[3] QIU, W., CHEN, B., TANG, L., *et al*., "Antibiotic chlortetracycline causes transgenerational Immunosuppression via NF-κB", *Environmental Science & Technology*, v. 56, n. 7, pp. 4251–4261, Apr. 2022. doi: http://doi.org/10.1021/acs.est.1c07343. PubMed PMID: 35286074.

[4] BI, Z., SONG, G., SUN, X., "Deciphering antibiotic resistance genes and microbial community of anammox consortia under sulfadiazine and chlortetracycline stress", *Ecotoxicology and Environmental Safety*, v. 234, pp. 113343, Apr. 2022. doi: http://doi.org/10.1016/j.ecoenv.2022.113343. PubMed PMID: 35259594.

[5] WANG, Y., HE, Y., LI, X., *et al*., "Enhanced biodegradation of chlortetracycline via a microalgae-bacteria consortium", *Bioresource Technology*, v. 343, pp. 126149, Jan. 2022. doi: http://doi.org/10.1016/j.biortech.2021.126149. PubMed PMID: 34673189.

[6] GOU, C., WANG, Y., ZHANG, X., *et al*., "Effects of chlorotetracycline on antibiotic resistance genes and the bacterial community during cattle manure composting", *Bioresource Technology*, v. 323, pp. 124517, Mar. 2021. doi: http://doi.org/10.1016/j.biortech.2020.124517. PubMed PMID: 33360947.

[7] GU, J., CHEN, C., HUANG, X., *et al*., "Occurrence and risk assessment of tetracycline antibiotics in soils and vegetables from vegetable fields in Pearl River Delta, South China", *The Science of the Total Environment*, v. 776, pp. 145959, Jul. 2021. doi: http://doi.org/10.1016/j.scitotenv.2021.145959.

[8] CONDE-CID, M., FERNÁNDEZ-CALVIÑO, D., NÚÑEZ-DELGADO, A., *et al*., "Estimation of adsorption/desorption Freundlich's affinity coefficients for oxytetracycline and chlortetracycline from soil properties: experimental data and pedotransfer functions", *Ecotoxicology and Environmental Safety*, v. 196, pp. 110584, Jun. 2020. doi: http://doi.org/10.1016/j.ecoenv.2020.110584. PubMed PMID: 32278142.

[9] MA, Y., WANG, S., GUO, J., *et al*., "Sensitive fluorescent detection of phosmet and chlortetracycline in animal-derived food samples based on a water-stable Cd(II) chain-based zwitterionic metal-organic framework", *Analytica Chimica Acta*, v. 1280, pp. 341850, Nov. 2023. doi: http://doi.org/10.1016/j.aca.2023.341850. PubMed PMID: 37858547.

[10] YI, K., XU, S., CHENG, H., *et al*., "A label-free sensor based on a carbon nanotube-graphene platform for the detection of non-Hodgkin lymphoma genes", *Alexandria Engineering Journal*, v. 84, pp. 93–99, Dec. 2023. doi: http://doi.org/10.1016/j.aej.2023.10.045.

[11] WANG, X., SHI, S., ZHANG, F., *et al*., "Application of a nanotip array-based electrochemical sensing platform for detection of indole derivatives as key indicators of gut microbiota health", *Alexandria Engineering Journal*, v. 85, pp. 294–299, Dec. 2023. doi: http://doi.org/10.1016/j.aej.2023.11.032.

[12] CHEN, L., ZHU, S., WANG, X., "Detection of glioma cells based on electrochemical sensor based on an aptamer method recognition", *International Journal of Electrochemical Science*, v. 17, n. 12, pp. 221258, Dec. 2022. doi: http://doi.org/10.20964/2022.12.59.

[13] LI, H., ZHANG, Y., FENG, K., *et al*., "Fabrication of graphene-assisted voltammetry platform for the detection of nitrate ions in PM2.5", *Carbon Letters*, v. 33, n. 7, pp. 2143–2152, Dec. 2023. doi: http://doi.org/10.1007/s42823-023-00585-1.

[14] RASHID, R., SHAFIQ, I., AKHTER, P., *et al*., "A state-of-the-art review on wastewater treatment techniques: the effectiveness of adsorption method", *Environmental Science and Pollution Research International*, v. 28, n. 8, pp. 9050–9066, Feb. 2021. doi: http://doi.org/10.1007/s11356-021-12395-x. PubMed PMID: 33483933.

[15] RATHI, B.S., KUMAR, P.S., "Application of adsorption process for effective removal of emerging contaminants from water and wastewater", *Environmental Pollution*, v. 280, pp. 116995, Jul. 2021. doi: http://doi.org/10.1016/j.envpol.2021.116995. PubMed PMID: 33789220.

[16] ULLAH, S., FAIZ, P., LENG, S., "Synthesis, mechanism, and performance assessment of zero-valent iron for metal-contaminated water remediation: a review", *Clean (Weinheim)*, v. 48, n. 9, pp. 2000080, 2020. doi: http://doi.org/10.1002/clen.202000080.

[17] KEN, D.S., SINHA, A., "Recent developments in surface modification of nano zero-valent iron (nZVI): Remediation, toxicity and environmental impacts", *Environmental Nanotechnology, Monitoring & Management*, v. 14, pp. 100344, Dec. 2020. doi: http://doi.org/10.1016/j.enmm.2020.100344.

[18] MANDAL, S., PU, S., SHANGGUAN, L., *et al*., "Synergistic construction of green tea biochar supported nZVI for immobilization of lead in soil: A mechanistic investigation", *Environment International*, v. 135, pp. 105374, Feb. 2020. doi: http://doi.org/10.1016/j.envint.2019.105374. PubMed PMID: 31864028.

[19] FAN, J., CHEN, X., XU, Z., *et al*., "One-pot synthesis of nZVI-embedded biochar for remediation of two mining arsenic-contaminated soils: arsenic immobilization associated with iron transformation", *Journal of Hazardous Materials*, v. 398, pp. 122901, Nov. 2020. doi: http://doi.org/10.1016/j.jhazmat.2020.122901. PubMed PMID: 32470770.

[20] MANDAL, S., PU, S., WANG, X., *et al*., "Hierarchical porous structured polysulfide supported nZVI/biochar and efficient immobilization of selenium in the soil", *The Science of the Total Environment*, v. 708, pp. 134831, Mar. 2020. doi: http://doi.org/10.1016/j.scitotenv.2019.134831. PubMed PMID: 31784164.

[21] MANDAL, S., PU, S., HE, L., *et al*., "Biochar induced modification of graphene oxide & nZVI and its impact on immobilization of toxic copper in soil", *Environmental Pollution*, v. 259, pp. 113851, Apr. 2020. doi: http://doi.org/10.1016/j.envpol.2019.113851. PubMed PMID: 31918134.

[22] MA, F., PHILIPPE, B., ZHAO, B., *et al*., "Simultaneous adsorption and reduction of hexavalent chromium on biochar-supported nanoscale zero-valent iron (nZVI) in aqueous solution", *Water Science and Technology*, v. 82, n. 7, pp. 1339–1349, Aug. 2020. doi: http://doi.org/10.2166/wst.2020.392. PubMed PMID: 33079714.

[23] HUANG, X., NIU, X., ZHANG, D., *et al*., "Fate and mechanistic insights into nanoscale zerovalent iron (nZVI) activation of sludge derived biochar reacted with Cr(VI)", *Journal of Environmental Management*, v. 319, pp. 115771, Oct. 2022. doi: http://doi.org/10.1016/j.jenvman.2022.115771. PubMed PMID: 35982569.

[24] XU, M., MA, X., CHEN, Y., *et al*., "Spectroscopic investigation of Cr(VI) sorption on nZVI/biochar composites", *Journal of Molecular Liquids*, v. 366, pp. 120262, Nov. 2022. doi: http://doi.org/10.1016/j.molliq.2022.120262.

[25] LI, S., YANG, F., LI, J., *et al*., "Porous biochar-nanoscale zero-valent iron composites: Synthesis, characterization and application for lead ion removal", *The Science of the Total Environment*, v. 746, pp. 141037, Dec. 2020. doi: http://doi.org/10.1016/j.scitotenv.2020.141037. PubMed PMID: 32745850.

[26] YANG, C., GE, C., LI, X., *et al*., "Does soluble starch improve the removal of Cr(VI) by nZVI loaded on biochar?", *Ecotoxicology and Environmental Safety*, v. 208, pp. 111552, Jan. 2021. doi: http://doi.org/10.1016/j.ecoenv.2020.111552. PubMed PMID: 33396093.

[27] LIU, S., ZHANG, S., FAN, M., *et al*., "High-efficiency adsorption of various heavy metals by tea residue biochar loaded with nanoscale zero-valent iron", *Environmental Progress & Sustainable Energy*, v. 40, n. 6, pp. e13706, 2021. doi: http://doi.org/10.1002/ep.13706.

[28] SHANG, X., YANG, L., OUYANG, D., *et al*., "Enhanced removal of 1,2,4-trichlorobenzene by modified biochar supported nanoscale zero-valent iron and palladium", *Chemosphere*, v. 249, pp. 126518, Jun. 2020. doi: http://doi.org/10.1016/j.chemosphere.2020.126518. PubMed PMID: 32213390.

[29] LIU, L., ZHAO, J., LIU, X., *et al*., "Reduction and removal of As(V) in aqueous solution by biochar derived from nano zero-valent-iron (nZVI) and sewage sludge", *Chemosphere*, v. 277, pp. 130273, Aug. 2021. doi: http://doi.org/10.1016/j.chemosphere.2021.130273. PubMed PMID: 33770694.

[30] ZHANG, Y., JIAO, X., LIU, N., *et al*., "Enhanced removal of aqueous Cr(VI) by a green synthesized nanoscale zero-valent iron supported on oak wood biochar", *Chemosphere*, v. 245, pp. 125542, Apr. 2020. doi: http://doi.org/10.1016/j.chemosphere.2019.125542. PubMed PMID: 31855758.

[31] HUANG, T., PAN, L., DONG, J., *et al*., "A comprehensive investigation of zeolite-rich tuff functionalized with 3-mercaptopropionic acid intercalated green rust for the efficient removal of HgII and CrVI in a binary system", *Journal of Environmental Management*, v. 324, pp. 116344, Dec. 2022. doi: http://doi.org/10.1016/j.jenvman.2022.116344. PubMed PMID: 36166867.

[32] BOSS, A.F.N., FERREIRA, H.R., BRAGHIROLI, F.L., *et al*., "Investigation of sustainable porous carbon as radar absorbing material", *Matéria (Rio de Janeiro)*, v. 26, n. 2, pp. e12963, May. 2021. doi: http://doi.org/10.1590/s1517-707620210002.1263.

[33] FAN, C., CHEN, N., QIN, J., *et al*., "Biochar stabilized nano zero-valent iron and its removal performance and mechanism of pentavalent vanadium(V(V))", *Colloids and Surfaces. A, Physicochemical and Engineering Aspects*, v. 599, pp. 124882, Aug. 2020. http://doi.org/10.1016/j.colsurfa.2020.124882.

[34] HUANG, T., SU, Z., DAI, Y., *et al*., "Enhancement of the heterogeneous adsorption and incorporation of uraniumVI caused by the intercalation of β-cyclodextrin into the green rust", *Environmental Pollution*, v. 290, pp. 118002, Dec. 2021. doi: http://doi.org/10.1016/j.envpol.2021.118002. PubMed PMID: 34419862.

[35] SONG, D., HUANG, T., LUO, Y., *et al*., "Nonthermal plasma-activated polyvalent cerium-manganese bimetallic (hydro)oxide-functionalized nanographene for the removal of thallium(I) contaminants and mechanism exploration", *Journal of Cleaner Production*, v. 429, pp. 139610, Dec. 2023. doi: http://doi.org/10.1016/j.jclepro.2023.139610.

[36] HUANG, T., SONG, D., ZHOU, L., *et al*., "Non-thermal plasma irradiated polyaluminum chloride for the heterogeneous adsorption enhancement of Cs^{+} and Sr^{2+} in a binary system", *Journal of Hazardous Materials*, v. 424, n. Pt B, pp. 127441, Feb. 2022. doi: http://doi.org/10.1016/j.jhazmat.2021.127441. PubMed PMID: 34673396.

[37] SILVA, H.D.M., ALCANTARA, G.U., DE SOUZA, L.Z.M., *et al*., "Produção e caracterização do biocarvão obtido de palha de cana-de-açúcar", *Matéria (Rio de Janeiro)*, v. 28, n. 4, pp. e20230218, Dec. 2023. doi: http://doi.org/10.1590/1517-7076-rmat-2023-0218.

[38] CHEN, A., WANG, H., ZHAN, X., *et al*., "Applications and synergistic degradation mechanisms of nZVI-modified biochar for the remediation of organic polluted soil and water: a review", *The Science of the Total Environment*, v. 911, pp. 168548, Feb. 2024. doi: http://doi.org/10.1016/j.scitotenv.2023.168548. PubMed PMID: 37989392.

[39] ZHAO, X., GAO, P., LIU, W., *et al*., "Research on the interface characteristics of coal gangue with different geosynthetic reinforcements", *Matéria (Rio de Janeiro)*, v. 29, n. 2, pp. e20240012, May. 2024. doi: http://doi.org/10.1590/1517-7076-rmat-2024-0012.

[40] HUANG, T., SONG, D., YANG, C., *et al*., "Nonthermal plasma-irradiated polyvalent ferromanganese binary hydro(oxide) for the removal of uranyl ions from wastewater", *Environmental Research*, v. 217, pp. 114911, Jan. 2023. doi: http://doi.org/10.1016/j.envres.2022.114911. PubMed PMID: 36427641.

[41] HUANG, P., ZHANG, P., WANG, C., *et al*., "P-doped biochar regulates nZVI nanocracks formation for superefficient persulfate activation", *Journal of Hazardous Materials*, v. 450, pp. 130999, May. 2023. doi: http://doi.org/10.1016/j.jhazmat.2023.130999. PubMed PMID: 36848845.

[42] LI, L., LI, J., YAN, Y., *et al*., "Removal of organophosphorus flame retardant by biochar-coated nZVI activating persulfate: Synergistic mechanism of adsorption and catalytic degradation", *Environmental Pollution*, v. 331, n. Pt 1, pp. 121880, Aug. 2023. doi: http://doi.org/10.1016/j.envpol.2023.121880. PubMed PMID: 37236590.

[43] XIN, Y., ZHANG, P., SHEN, J., *et al*., "Development of vitamin B6-mediated biochar with nano zero-valent iron coating for oxytetracycline removal through adsorption and degradation under harsh acidic conditions", *Water (Basel)*, v. 14, n. 17, pp. 2734, Jan. 2022. doi: http://doi.org/10.3390/w14172734.

[44] YANG, L., CHEN, Y., OUYANG, D., *et al*., "Mechanistic insights into adsorptive and oxidative removal of monochlorobenzene in biochar-supported nanoscale zero-valent iron/persulfate system", *Chemical Engineering Journal*, v. 400, pp. 125811, Nov. 2020. doi: http://doi.org/10.1016/j.cej.2020.125811.

[45] GAO, J., HAN, D., XU, Y., *et al*., "Persulfate activation by sulfide-modified nanoscale iron supported by biochar (S-nZVI/BC) for degradation of ciprofloxacin", *Separation and Purification Technology*, v. 235, pp. 116202, Mar. 2020. doi: http://doi.org/10.1016/j.seppur.2019.116202.

[46] LIU, M., ZOU, D., MA, T., *et al*., "Stable cellulose-based porous binary metal-organic gels as highly efficient adsorbents and their application in an adsorption bed for chlortetracycline hydrochloride decontamination", *Journal of Materials Chemistry. A, Materials for Energy and Sustainability*, v. 8, n. 14, pp. 6670–6681, Apr. 2020. doi: http://doi.org/10.1039/C9TA13818H.

[47] LIANG, X., LIU, L., JIANG, Y., *et al*., "Study of the sorption/desorption behavior of chlortetracycline on sediments in the upper reaches of the Yellow River", *Chemical Engineering Journal*, v. 428, pp. 131958, Jan. 2022. doi: http://doi.org/10.1016/j.cej.2021.131958.